Applied Catalysis B: Environmental 301 (2022) 120803

Contents lists available at ScienceDirect

Applied Catalysis B: Environmental

journal homepage: www.elsevier.com/locate/apcatb

Cu^{+}–Ti^{3+} interface interaction mediated CO_2 coordination model for controlling the selectivity of photocatalytic reduction CO_2

Zhi-wen Wang, Ying-zhang Shi, Cheng Liu, Yue-yue Kang, Ling Wu *

State Key Laboratory of Photocatalysis on Energy and Environment, College of Chemistry, Fuzhou University, Fuzhou 350116, China

ARTICLE INFO

Keywords:
Cu_2O clusters
TiO_2 nanosheet
Photoreduction CO_2
Coordination

ABSTRACT

Cu_2O clusters/TiO_2 nanosheet (CNSX) as a photocatalyst is created to tailor the selectivity of CO_2 photoreduction. The catalysts show different selectivity of CO and CH_4 with the increase of Cu_2O mass. TiO_2 nanosheet (NS) exhibits 100% selectivity of CH_4 with a rate of 37.6 μmol g^{-1} h^{-1}. However, CO_2 would be converted to CO with selectivity of 98% and yield of 162.6 μmol g^{-1} h^{-1} on 5 wt% Cu_2O/TiO_2 nanosheet (CNS3). The Ti···CO_2^-···Ti coordination intermediate on Ti^{3+} sites is responsible for CH_4 formation, whereas the Cu···CO_2···Ti specie on $Cu^{1-\delta}$ and $Ti^{4+\delta}$ sites determines CO production. The Cu^{+}–Ti^{3+} interface interaction on CNSX surface can generate $Cu^{1-\delta}$ and $Ti^{4+\delta}$ sites and eliminate Ti^{3+} via the charge transfer from Ti^{3+} to Cu^{+}. The selectivity is thus tailored effectively by Cu^{+}–Ti^{3+} interface interaction mediated CO_2 coordination model. This work would offer a new perspective for tailoring the selectivity of CO_2 photoreduction.

1. Introduction

Conversion of CO_2 to the value-added chemicals or fuels as a sustainable path could help to decrease the reliance on fossil fuels, mitigate energy crisis and environment issues [1–3]. Artificial photosynthesis of fuels from CO_2 by using photocatalysts has already become a research focus in recent years due to conversion of solar energy to the direct utilization chemical energy [4,5]. Because CO_2 can be converted to multitudinous products, such as CO, HCOOH, CH_3OH, CH_4 and some C_2 products (C_2H_4, C_2H_6, CH_3CH_2OH), tailoring the products selectivity has been always an urgent and significant task [6–10]. Taking CH_4 and CO as samples, though CO_2 can be converted to a single product on some catalysts, so far, few effective strategies could achieve the accurate control for selectivity [11,12]. It is reported that some factors could influence the selectivity, such as band structure, separation efficiency of electrons-holes, surface active sites and activation of reactants [13]. Moreover, the coordination mode is a crucial factor for the selectivity of products, which may offer a possible chance about governing the products selectivity via tailoring the coordination modes. The coordination modes are closely related to the property of active sites [14]. Thus, a key path is to tailor the active sites for selectively bonding CO_2 by creating a special catalyst.

Our previous work found that a single component catalyst contained surface M1 atoms with unpair electrons would bond CO_2 via forming the bridging M···CO_2^-···M species, which is beneficial to produce CH_4 [15]. So, we just need to create another model which determines to generate CO. However, a transition metal oxide catalyst with single component only possesses the identified active site (M1), which restricts modulation of coordination model. It is necessary to introduce the new active site. Constructing composite catalyst is a widely used method, which can optimize the catalyst properties and particularly provide multi active sites [16]. Because an excess of active sites may cause that to investigate reaction mechanisms in photocatalysts develops very difficult, the composite materials with two metal sites (M1and M2) are created as the target photocatalyst. Therefore, to understand which possible coordination mode would be generated on catalyst surface becomes a key step.

Based on Lewis theory of acids (LA) and bases (LB), four combination patterns for M1 and M2 may appear on catalyst: I. M1 and M2 (both of LA); II. M1and M2 (both of LB); III. M1 and M2 (both of LA and LB); Ⅳ. M1(LA) and M2 (LB). In this case, Scheme 1 shows four possible coordination modes. For route I, both of M1 and M2 serve as Lewi acid centers to bond with O via the coordination of the lone pair electron of oxygen atom to empty d orbital of the metal. Intermediate-I is a μ_2-η^2 coordination mode with two O→M bonds via transferring the lone pair electron of oxygen atom to empty d orbital of the metal, facilitating to form HCOOH. Route II exhibits that both of M1 and M2 are considered as Lewi base centers to bind with C through transferring unpaired electron coordination to lowest-unoccupied molecular orbital (2πu

* Corresponding author.
E-mail address: wuling@fzu.edu.cn (L. Wu).

https://doi.org/10.1016/j.apcatb.2021.120803
Received 26 July 2021; Received in revised form 14 September 2021; Accepted 7 October 2021
Available online 9 October 2021

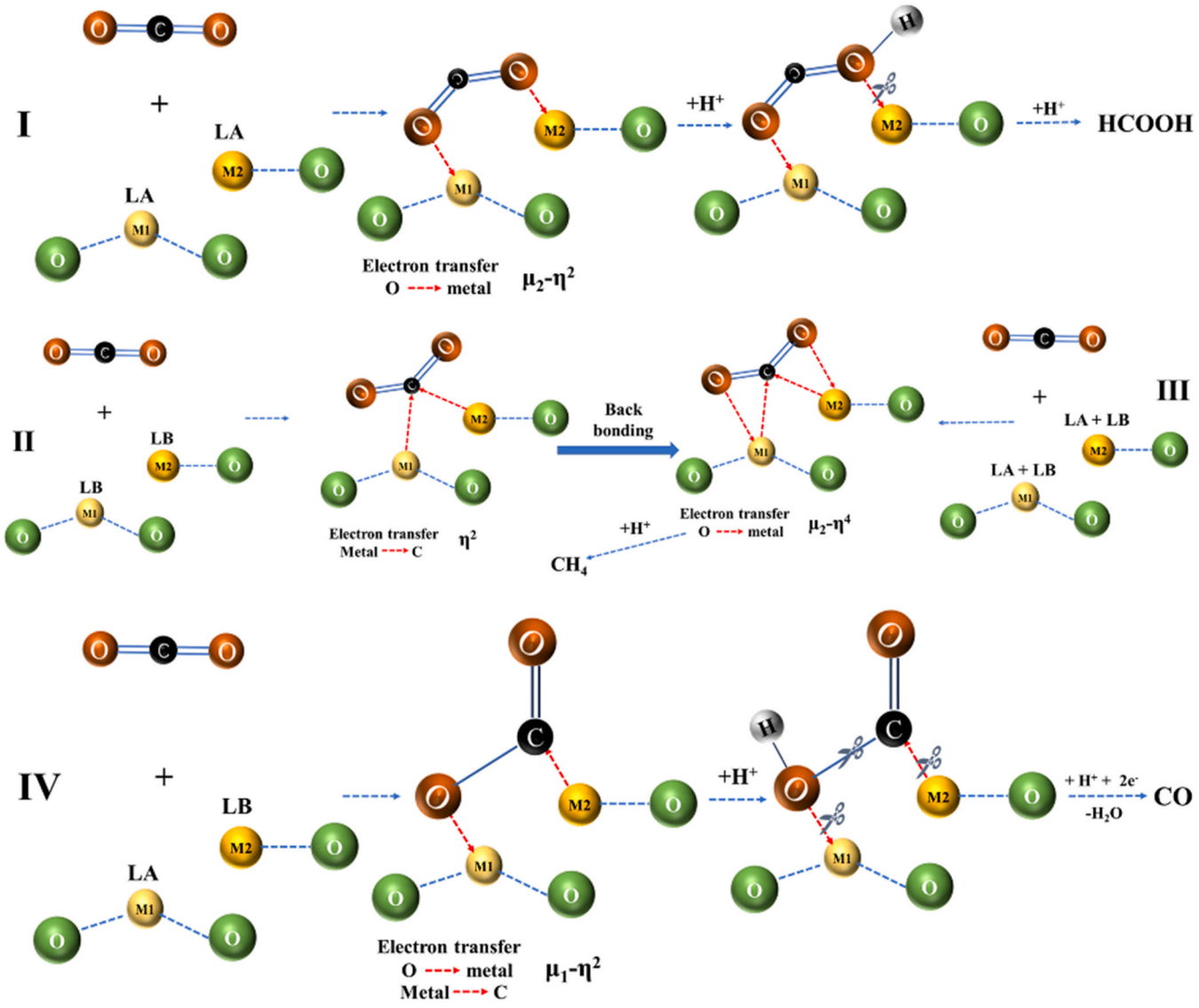

Scheme 1. Manipulating the products selectivity by tailoring coordination mode. Photoreduction of CO_2 on the catalyst: I. M1 and M2 (both of LA); II. M1 M2 (both of LB); III. M1and M2 (both of LA and LB); Ⅳ. M1(LA) and M2 (LB). M represents the metal site, '$H^+ + e^-$' refers to the proton coupled electron transfer process and '-H_2O' means the desorption of H_2O molecules after the intermediates react with the proton–electron pair.

LUMO) of CO_2. But this mode is unreasonable due to the formation back bonding, which would be translated to a higher hapticity (μ_2-η^4) mode (Intermediate-III). Intermediate-III is a bridging M1···CO_2^-···M2 species, which promotes CH_4 production in our previous work. Moreover, path Ⅳ(intermediate-Ⅳ) depicts that M1 and M2 play Lewi base and Lewi base respectively, which bond CO_2 via forming the M1→C and O→M2 bonds. In this μ_1-η^2 species, the electron of M1 is transferred to C and then the electron of O (CO_2) is transferred to M2 via back bonding. It implies that the activated CO_2 molecule may obtain little charge due to the two different directions of electron transfer, which would impede the C atom protonation. So, only one coordinated C═O bond is easy to be dissociated for producing CO. According to the above discussion, it is one of the valid steps for regulating the selectivity of CO and CH_4 that the bridging M···CO_2^-···M and the bimetal bridging M1···CO_2···M2 modes are tailored via creating the catalyst with M1(LA) and M2 (LB) sites.

TiO_2 with ultrathin morphology is an attractive photocatalyst due to the larger surface area, faster electrons-holes separation and more exposed surface Ti atoms, which could serve as an ideal material to prepare a composite catalyst [17–19]. Cu_2O is a promising photocatalyst owing to the unique optical property, nontoxic nature and low price, which has been widely used to develop composite catalyst, such as Cu_2O/TiO_2 [20,21], Cu_2O/ZnO [22], Cu_2O/rGO [23], Cu_2O@h-BN [24], Cu_2O/NH_2-MIL-125(Ti) [25]. Therefore, Cu_2O is one of the best catalysts to optimize the TiO_2 nanosheet properties and provide Cu site. Cu_2O/TiO_2 has been widely used to photocatalytic reduction CO_2 [26–28]. Particularly, Cu compounds possess good multielectron transfer properties, facilitating the charge transfer between Cu site and Ti site [29]. It means that the different properties of (LB and LA) Cu and Ti site may be generated on catalyst. Therefore, it is a feasible way to design Cu_2O/TiO_2 nanosheet for achieving the controllable selectivity of CO and CH_4. Moreover, many works devote to explore the quantum efficiency for enhance activity, such as heterojunction effect [29]. However, few works were focused on the interaction of surface/interface among CO_2, Cu_2O and TiO_2. To investigate the interaction of surface/interface in a catalytic process is a significant challenge, particularly when the photocatalysts possess multi-components.

Herein, Cu_2O clusters (~ 2 nm) were prepared by a neoteric and handy method that metallic cooper was oxidized under air and then peeled the surface oxide film. Subsequently, we prepared Cu_2O clusters

decorated TiO_2 nanosheet with a thickness of 3.2 nm as a photocatalyst for CO_2 photoreduction. The morphology and structure of the catalyst were well characterized by XRD, SEM, TEM, AFM, and BET. The photoelectrochemical properties of the samples were evaluated by the transient photocurrent responses, electrochemical impedance spectroscopy and fluorescence spectrum. The XPS and EPR results revealed that Cu_2O clusters/TiO_2 nanosheet contains electron-enriched Cu and electron-deficient Ti sites which would play LB and LA sites, respectively. The results of XPS, TPD, in situ EPR and in situ FT-IR indicated the Cu and Ti site promoted the formation of bimetal bridging M1···CO_2···M2 coordination model which further facilitated CO generation. The DRS results manifested that the samples can increase visible light absorption due to the CO_2 absorption. Under light irradiation, the catalyst with different Cu_2O loading mass exhibited a special selectivity for CH_4 or CO. Besides, a multi synergistic effect among Cu_2O clusters, TiO_2 nanosheet, coordination activation and photocatalysis was deeply revealed at a molecule level.

2. Experimental section

2.1. Preparation of the Cu_2O clusters and Cu_2O/TiO_2 nanosheets (CNSX)

TiO_2 nanosheets (NS) were prepared by a reported method in supporting information [30]. The Cu_2O clusters were prepared by a handy method. The copper rod (99.99%, r = 2 mm) was placed in a 250 mL bottle, and then mixture gas (N_2:78%; O_2:22%) has been injected continuously for 30 days. Next, 200 mL of ultrapure water was added in the bottle to sonicate in ultrasonic bath (KQ3200DA) for 2 h. The upper layer turbid liquid was collected after centrifugation (at 1000 rpm) for 1 min. The turbid liquid was centrifugated (at 10,000 rpm) to produce brown powder and then dried at 60 ℃. A series of Cu_2O/TiO_2 nanosheets were prepared by physical mixture and then ultrasound treatment. The samples labels as follows: 1 wt% Cu_2O/TiO_2 (CNS1), 3 wt% Cu_2O/TiO_2 (CNS2) and 5 wt% Cu_2O/TiO_2 (CNS3), respectively. Moreover, 7 wt% Cu_2O/TiO_2 (CNS4), 9 wt% Cu_2O/TiO_2 (CNS5) and 12 wt% Cu_2O/TiO_2 (CNS6) were only prepared to evaluate the photocatalytic performances.

2.2. The CO_2 adsorbed catalysts measurement

100 mg of a catalyst was dispersed in 20 mL of pure water by sonication to get pulp suspension. Then the CO_2 adsorbed catalysts (Cas) were prepared by cryodesiccation of pulp suspension under vacuum. Cas was detected by using DRS and XPS. A Brucker A300 spectrometer was used to detect the Electron spin resonance (EPR) signals. 20 mg of the powder sample was put into an EPR quartz tube and treated under dynamic vacuum (4.5 Pa). Then CO_2 gas was put into the tube for recording in situ EPR spectra. Nicolet IS50 Fourier transform infrared (FT-IR) spectrometer with an in-situ reactor was adopted to record in situ diffuse reflection infrared spectroscopy of CO_2 adsorbed samples. 100 mg of a sample was pressed into the reactor. The reactor was treated under dynamic vacuum (4.5 Pa) for 2 h at 200 ℃ to remove surface adsorption species. Then, CO_2 gas was put into the reactor to record the in situ FTIR spectra.

2.3. Photocatalytic CO_2 reduction measurement

The CO_2 photoreduction experiments were performed in a 45 mL glass bottle at ambient temperature (Fig. S1). 10 mg of catalyst was dispersed in 20 mL of pure water by sonication to get pulp suspension. This system was treated with vacuum degassing and then refilled with pure CO_2 gas (99.999%) for 5 times. The photocatalytic reaction was carried out for 6 h with UV–vis–light irradiation (PLS-SXE300D, 1000 mW/cm^2, Beijing Perfectlight Co., Ltd. $\lambda \geq 360$ nm). After photoreaction, 0.4 mL of mixed gas was taken from the reactor to analyze the gas concentration of the product using a gas chromatography (GC-7890B, Agilent) equipped with a TCD, an FID detector and a chromatographic column (MolSieve 5 A). The isotopic $^{13}CO_2$ experiment was analyzed by an Agilent GC–MS analyzer with 5977B MSD mass spectrometer.

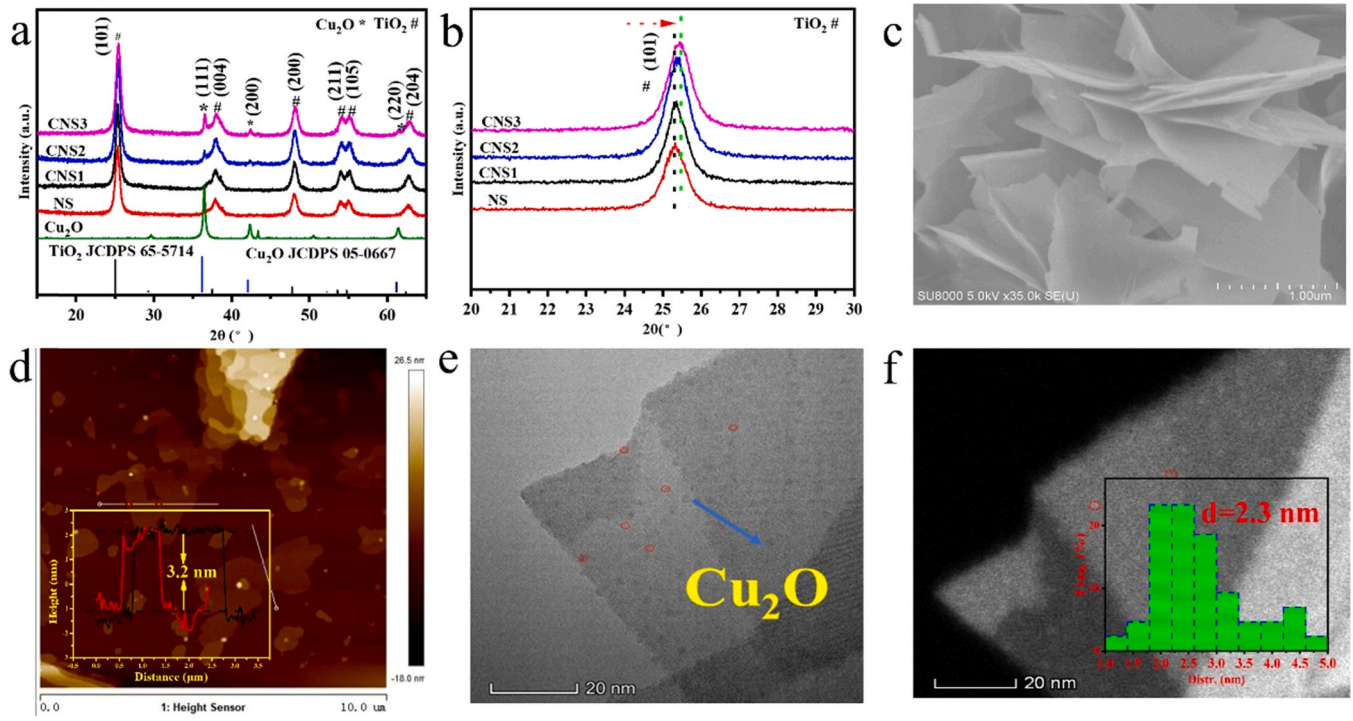

Fig. 1. (**a**) XRD patterns of the prepared samples and (**b**) the corresponding expanded XRD plots from 20° to 30°; (**c**) SEM image of NS; (**d**) AFM image of CNS3 and the height profiles corresponding to the AFM image in inset; TEM (**e**) and HADDF (**f**) images of CNS3 and size distribution of Cu_2O clusters in inset.

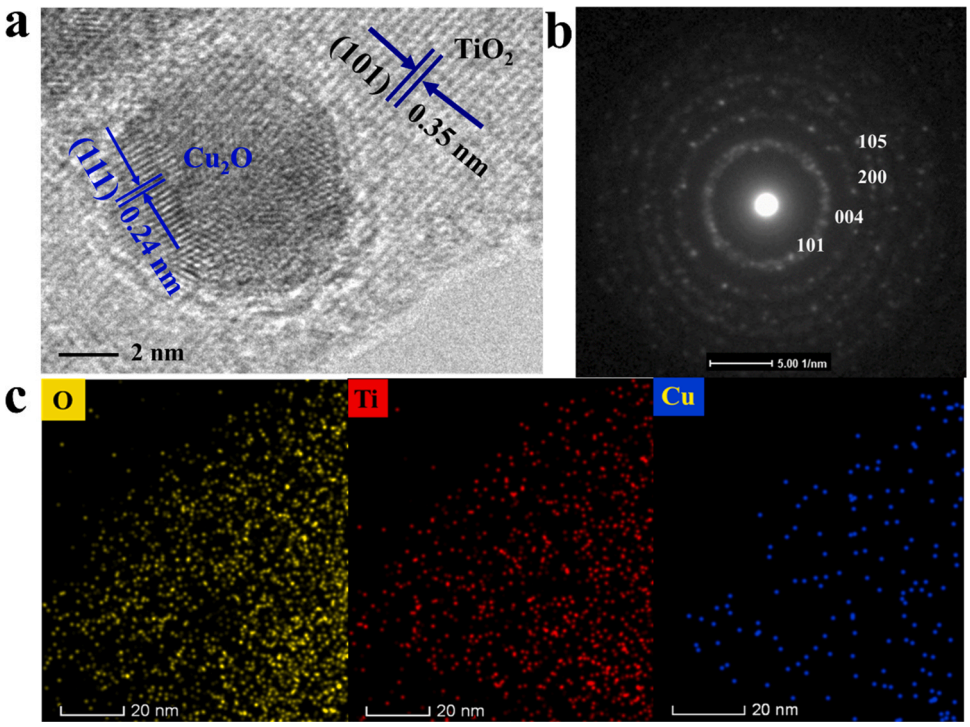

Fig. 2. (**a**) HRTEM image of CNS3; (**b**) SAED pattern of CNS3. (**c**) Mapping images of CNS3.

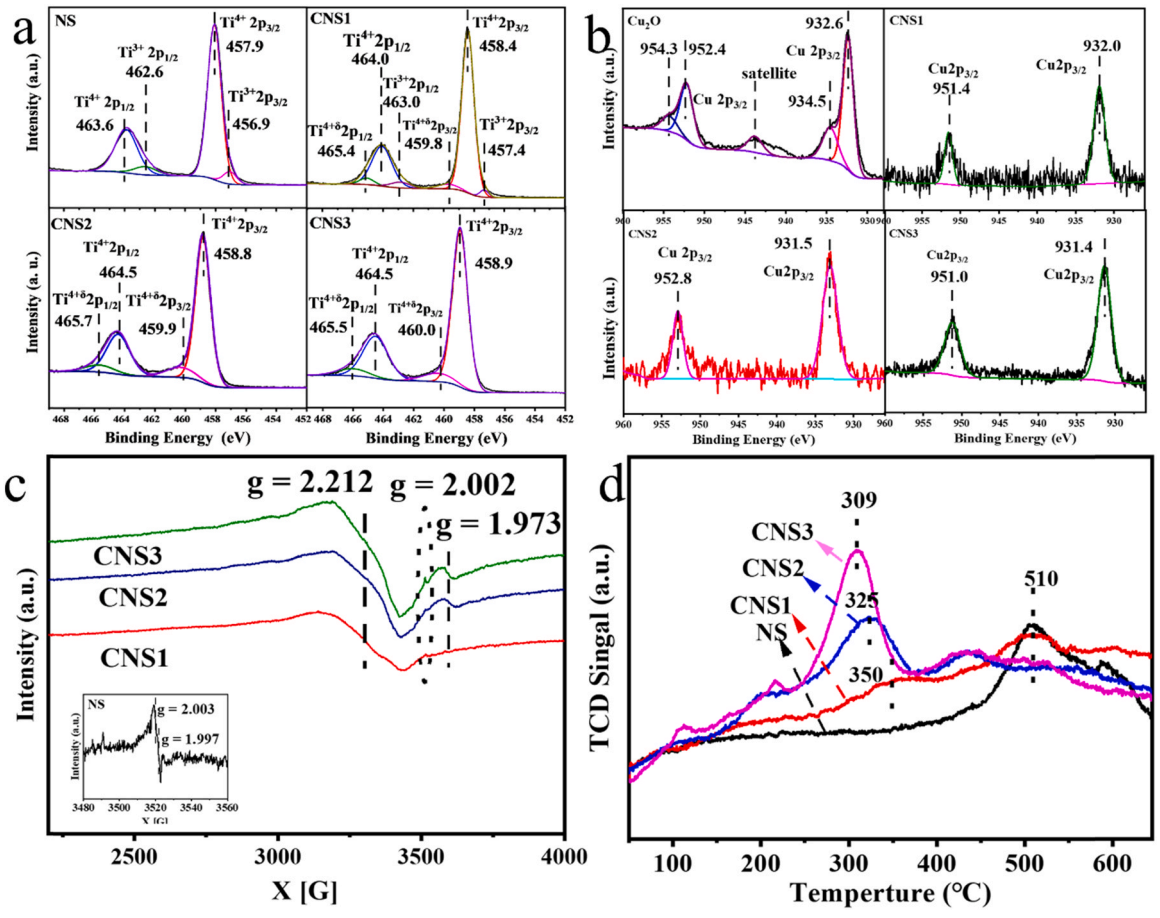

Fig. 3. (a)Ti 2p and (b) Cu 2p XPS spectra of the prepared catalysts; (c) EPR spectra of the samples; (d) The H_2-TPR profiles of the catalysts.

3. Result and discussion

3.1. Characterization of the prepared samples

The powder X-ray diffraction (XRD) was adopted to determine the crystal phases of the prepared samples. As shown in Fig. 1a, the diffraction patterns of all samples show the characteristic diffraction peaks of anatase TiO_2 (JCPDS No: 65–5714) [31]. The diffraction patterns of CNSX display three diffraction peaks at 36.4°, 42.3° and 61.4° can be well assigned to the (111), (200) and (220) crystal facets of cubic Cu_2O (JCPDS No: 05–0667), suggesting that the samples consist of the Cu_2O/TiO_2(anatase) [32]. In addition, a small shift to high angle of the lattice plane (101) is observed in the diffraction patterns of CNSX (Fig. 1b) compared to NS, inferring that the strong interaction between Cu_2O and TiO_2 [33]. The prepared catalysts with an ultra-thin structure (~3.2 nm) could be demonstrated by SEM, TEM and AFM images in Fig. 1c, d and e. The DRS spectra (Figure. S2a) depict that the Cu_2O sample spectrum has an obvious blue shift compared with spectrum of standard Cu_2O due to quantum scale effect, suggesting that the diameter of Cu_2O is up to nanoscale. Furthermore, a high dispersed nano-clusters with 2 nm diameter can be obviously found in the TEM and HADDF images (Fig. 1e and f). The HRTEM image (Fig. 2a) exhibits two kinds of the lattice stripes with 0.35 and 0.24 nm, corresponding to the lattice planes (101) of anatase TiO_2 and (111) of Cu_2O, respectively [34–36]. The distinct selected area electron diffraction (SAED) pattern (Fig. 2b) shows the polycrystalline anatase phase of the sample. In addition, mapping images (Fig. 2c) further reveal that the Cu element is uniformly distributed on the TiO_2 nanosheets. So, it means that the Cu_2O clusters/TiO_2 ultrathin nanosheets (CNSX) with a thickness of 4 TiO_2 cells are successfully created [37].

N_2 adsorption-desorption isotherm (Figure. S2b) reveals that the specific surface area of all the samples is about 90 m^2/g, which may offer abundant active sites on the surface to adsorb more CO_2 molecule for improving the photocatalytic activity [38]. The separation and transfer ability for photogenerated electrons-holes of the prepared samples was valued by the transient photocurrent response, electrochemical impedance spectroscopy (EIS), and PL (Figure. S3 a, b and c). The photo-response current of the catalysts (NS: 11.5, CNS1: 22.3, CNS2: 40.2 and CNS3: 49.3 $\mu A \cdot cm^{-2}$) gradually increase with adding the loading-mass of Cu_2O, revealing that Cu_2O could accelerate the separation and transfer ability for carries [39]. The EIS and PL analysis also can give an assistance for this result [40]. It may be attributed to the generated direct Z-scheme heterostructure in Fig. S12 [41].

The X-ray photoelectron spectroscopy (XPS) was used to detect the chemical composition and the chemical state of each element for unveiling whether the preconceived active sites are exposed on the prepared samples. The XPS survey (Figure. S4a) shows that Ti, O and Cu elements can be detected in CNSX, suggesting that Cu_2O is loaded on TiO_2 nanosheets successfully. The high-resolution Ti 2p spectra are displayed in Fig. 3a. The peaks of NS spectrum at 463.6 eV, 457.1 eV and 462.6 eV, 456.9 eV are corresponded to Ti^{4+} $2p_{1/2}$, $Ti^{4+}2p_{3/2}$ and Ti^{3+} $2p_{1/2}$, $Ti^{3+}2p_{3/2}$, respectively [42]. However, in the spectra of CNSX, the intensity of Ti^{3+} characteristic peaks gradually weakens and until disappears. Particularly, the Ti 2p spectra of CNSX can be fitted by added a group of peaks with higher binding energy (CNS1: 465.4 eV, 459.8 eV, CNS2: 465.7 eV, 459.9 eV and CNS3: 465.5 eV, 456.0 eV), which may be assigned to $Ti^{4+\delta}$ $2p_{1/2}$ and $Ti^{4+\delta}$ $2p_{3/2}$ [43]. It means that $Ti^{4+\delta}$ sites may act as the electron-deficient Ti sites (LA). Moreover, the electron binding energy of Ti in CNSX increases compared with that of in NS, demonstrating that Ti would loss electrons. The high-resolution Cu2p (Fig. 3b) and CuLMM spectra (Figure. S4b) of the samples depict the chemical state of Cu. A group of main peaks at 932.6 and 952.4 eV are observed in the spectra of Cu_2O, belonging to Cu^+/Cu^0 $2p_{1/2}$ and $2p_{3/2}$. A peak at 916.6 eV is showed in CuLMM spectra, identifying that the Cu chemical state is Cu^+ [44]. Moreover, a small group of peaks at 934.5 and 954.3 eV could be assigned to Cu^{2+} $2p_{1/2}$ and $Cu^{2+}2p_{3/2}$, respectively [45]. The XPS spectra of CNSX exhibit a single group of peaks at 932.0, 951.4 eV (CNS1), 931.5, 952.8 eV (CNS2) and 931.4, 951.0 eV (CNS3). According to the CuLMM spectra, the chemical state of Cu in the CNSX is considered as Cu^+. Compared with the binding energy of Cu in NS, a large shift toward the low-binding-energy side is observed in CNSX, suggesting that the electrons density of Cu increases greatly. Therefore, the electron-rich $Cu^{1-\delta}$ as a LB site may be appeared on CNSX. These XPS results reveal that the Cu^+-Ti^{3+} interface interaction may be generated via the charge transfer from Ti to Cu, which further causes the formation of electron-deficient $Ti^{4+\delta}$ sites (LA) and electron-rich $Cu^{1-\delta}$ (LB) sites on CNSX. The O chemical state of the samples is revealed by the high-resolution O1s XPS spectra (Figure. S4c, and d). The spectra could be deconvoluted into three peaks, which is identified as lattice oxygen (O1), hydroxyl (O2) and adsorbed oxygen (O3), respectively [46]. EPR was used to further reveal the active sites (Fig. 3c). NS possess some Ti^{3+}, which could be inferred from the peaks at g value of 2.003 and 1.997 [47]. The peak at g value of 2.212 belongs to the Cu^{2+} defects with unpaired electrons in 3d orbitals. In additional, the peak at g value of 2.002 could be considered as the metallic Cu clusters because Cu^+ obtains electrons from Ti^{3+} [42]. The peak at g value of 1.973 may be assigned to the unpaired electrons of other species formed by the charge transfer [48]. This result may provide additional evidence for the Cu^+-Ti^{3+} interface interaction.

Temperature programmed reduction (TPR) was carried out under H_2 atmosphere to further clear the type of metal oxide species and the interaction of Cu_2O with TiO_2. The H_2-TPR profiles of the catalysts are presented in Fig. 3d. The reduction profile of NS shows a main peak at 510 ℃ which might be attributed to the reduction of unsaturated Ti (such as Ti^{3+}) [49]. The peaks intensity at 510 ℃ of CNSX reduction profile gradually weaken, which may be considered as the decrease of Ti^{3+} content. Moreover, three main peaks at 350(CNS1), 325(CNS2) and 309 ℃ (CNS3) are observed in the profile, assigning to the reduction of Cu^+ [50]. The lowered reduction temperature reveals that the reduction Cu^+ becomes easier, inferring that the Cu^+ site obtain electrons from the Ti^{3+} site [51]. These results further confirm that the electron-deficient $Ti^{4+\delta}$ sites (LA) and electron-rich $Cu^{1-\delta}$ (LB) sites is created successfully on CNSX.

3.2. Performances of the prepared catalysts

To verify whether the photocatalyst could exhibit the desired results, the performances of catalysts about photoreduction CO_2 were carried out in atmospheric pressure under Xe light irradiation without any sacrificial reagents under ($\lambda \geq 360$ nm) light irradiation. As shown in Fig. 7a, NS exhibits a high CH_4 yield (37.6 $\mu mol\ g^{-1}\ h^{-1}$) with a near 100% selectivity. However, when Cu_2O is loaded, CO as a product is appeared. Two products of CH_4 (46.3 $\mu mol\ g^{-1}\ h^{-1}$, 72%) and CO (19.8 $\mu mol\ g^{-1}\ h^{-1}$, 28%) are generated on CNS1. The increase of CH_4 activity may be assigned to the improved the separation and transfer of the photogenerated carries by Cu_2O loaded on CNS1. With the increase of Cu_2O mass, the selectivity and activity of CO are gradually raised, whereas the yield of CH_4 gradually decreases. CNS3 shows the highest yield of CO (162.6 $\mu mol\ g^{-1}\ h^{-1}$, 98%). It is obvious that introducing Cu_2O could improve the yield of CO, which may be attributed to the variation of CO_2 coordination mode. To further explore the optimal mass of loaded Cu_2O, the catalysts with more Cu_2O were prepared for photoreduction CO_2. 7 wt% Cu_2O/TiO_2 (CNS4) still exhibits a high selectivity of CO (96.5%). However, H_2 as a product is appeared with a selectivity of 3.5%. The yield of H_2 is kept for boosting when Cu_2O mass is further increased. The selectivity of H_2 is up to 97.2% on 12 wt% Cu_2O/TiO_2 (CNS6). Therefore, 5% wt and 7% wt Cu_2O may be the best loaded mass for optimal yield of CO.

Moreover, in the Table S1, all the catalysts exhibit negligible photocatalytic activity in the absence of either H_2O or light irradiation, indicating that the products (CH_4 and CO) are originated from CO_2 reduction. CO_2 was replaced by isotope $^{13}CO_2$ to further confirm that the

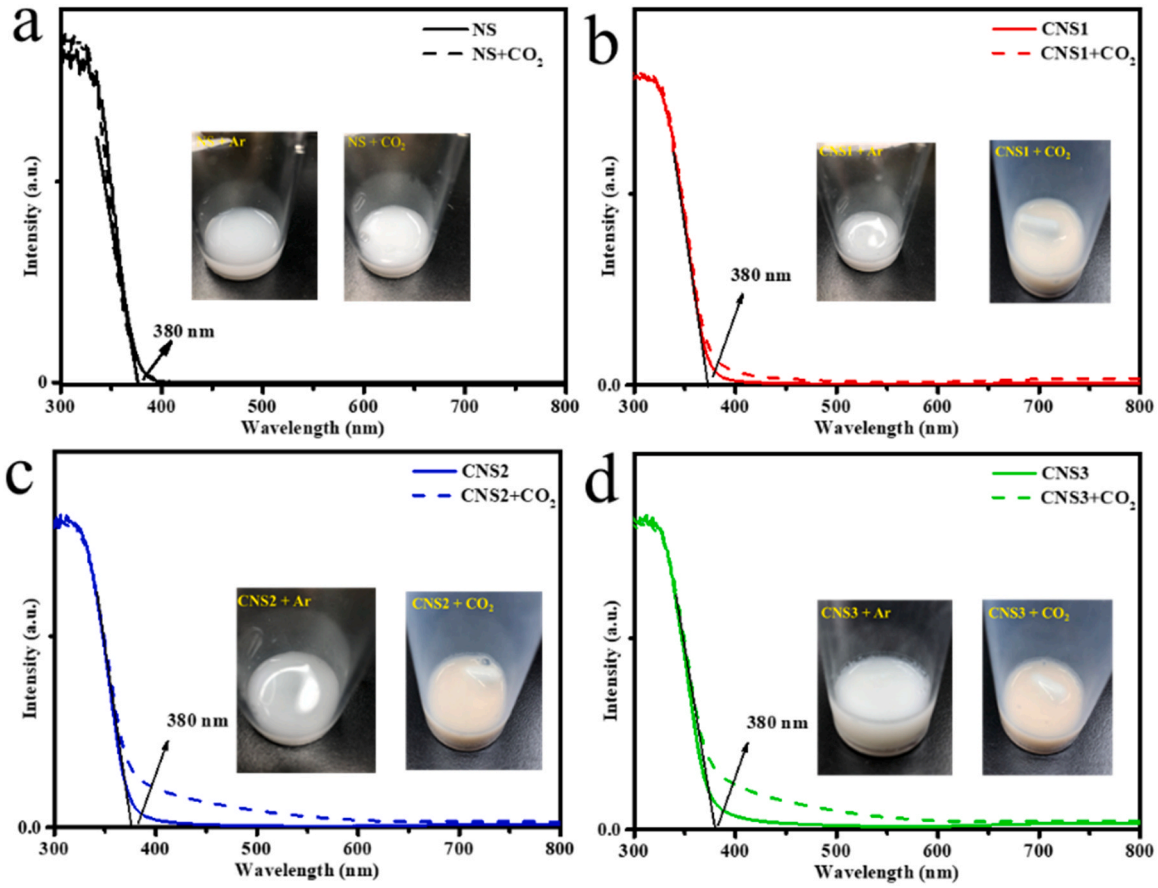

Fig. 4. DRS of the samples before and after adsorption of CO_2.

CH_4 and CO are produced by CO_2 photoreduction. In GC–MS results (Fig. 7b), the peak at the retention time of 0.7 and 1.7 min are belonged to ^{13}CO ($m/z = 29$) and $^{13}CH_4$ ($m/z = 17$) respectively, indicating the generated products from CO_2 reduction.

As an example, the stability of CNS3 was investigated via a 36-hours tests (Fig. S5). CNS3 can keep better yield of CO. To further explore the photostability of CNS3, the used photocatalyst is characterized by XRD, SEM, TEM (Fig. S6), and XPS (Fig. S7). These analyses show that the morphology structure and chemical property of the catalyst have negligible change. So, the catalysts keep the better photocatalytic stability.

3.3. Coordination of CO_2

To unveil why the products selectivity of CH_4 and CO can be tailored, the coordination behavior of CO_2 on the catalysts has been explored through a serious of in situ characterization analysis. DRS was used to determine the catalyst optical property. The loaded Cu_2O increase a little visible light sorption of the catalysts (Fig. S8). Furthermore, a special experimental phenomenon is observed when the CO_2 was injected into the reaction bottle with catalyst (CNSX) suspension. As shown in Fig. 4 **inset**, the color of CNSX would become yellow due to injected CO_2 but the catalysts keep white under Ar, showing that the adsorbed CO_2 would make the catalysts yellowing. Fig. 4a, b, c and d shows that CNSX could expand the absorption of visible light after absorption CO_2 because a charge transfer band between CO_2 and catalyst may be generated to absorb visible light [52,53]. It means that abundant CO_2 molecules would be coordinated on the catalysts via the charge transfer, which would enhance the activity of CO_2 photoreduction.

XPS was adopted to uncover the interaction between CO_2 and the active sites (Cu and Ti) via detecting the chemical state of each element in the catalysts after adsorption of CO_2. As shown in Fig. S9, the high resolution C1s spectra of the catalysts reveal that only adventitious carbon peaks at 284.8 eV. After adsorption CO_2, two peaks with higher binding energy (286.4 and 288.4 eV) can be added into the C1s spectra (Fig. 5a), which may be assigned to C-O and C═O of the adsorbed CO_2, respectively. It is obvious that C-O components increase in CNSX, suggesting that the coordination mode of CO_2 may possess C-O bonds. Moreover, in Fig. 5b, the O1s spectra show that intensity of the peaks at about 532.0 obviously increase, corresponding to the C═O or C-O of the adsorbed CO_2. The high resolution Ti2p spectra (Fig. 5c) show that the signals of $Ti^{4+\delta}$ disappear in CNSX after adsorption CO_2. Meanwhile, the binding energy of Ti shifts toward to the lower binding energy, suggesting that the electron density of Ti increase. It could be concluded that Ti sites may obtain additional electrons from CO_2. Fig. 5d shows that the Cu binding energy in CNSX is higher than that of the catalysts after adsorption CO_2, inferring that the electron density of Cu decreases. It indicates that the electrons of Cu sites may be transferred into CO_2. To further investigate binding and electron transfer between active sites and CO_2 molecules, in situ EPR measurement is carried out. The CO_2 adsorption on NS were explored in our previous work. So, the EPR spectra of CNSX before and after the adsorption of CO_2 are displayed in Fig. 6a. The g and A tensors ($A_{\parallel}$ for Cu of 137 G and $g_{\parallel}$ of 2.342) appear in spectra after adsorption CO_2, demonstrating that CO_2 would be bind on the catalyst via the formation of Cu complex [54]. The peak at 1.973 disappear, revealing that the unpaired electrons were redistributed on the catalysts surface due to the adsorbed CO_2 [55]. The Cu clusters signals at 2.002 also become weak after adsorption CO_2, which may be attributed to the electrons transfer from Cu to CO_2. Therefore, it determines that CO_2 molecule would be coordinated on the catalysts via the electrons transfer from $Cu^{1-\delta}$ to CO_2 and CO_2 to $Ti^{4+\delta}$. Therefore, the bimetal bridging Cu···CO_2···Ti intermediate (μ_1-η^2) may be formed on CNSX.

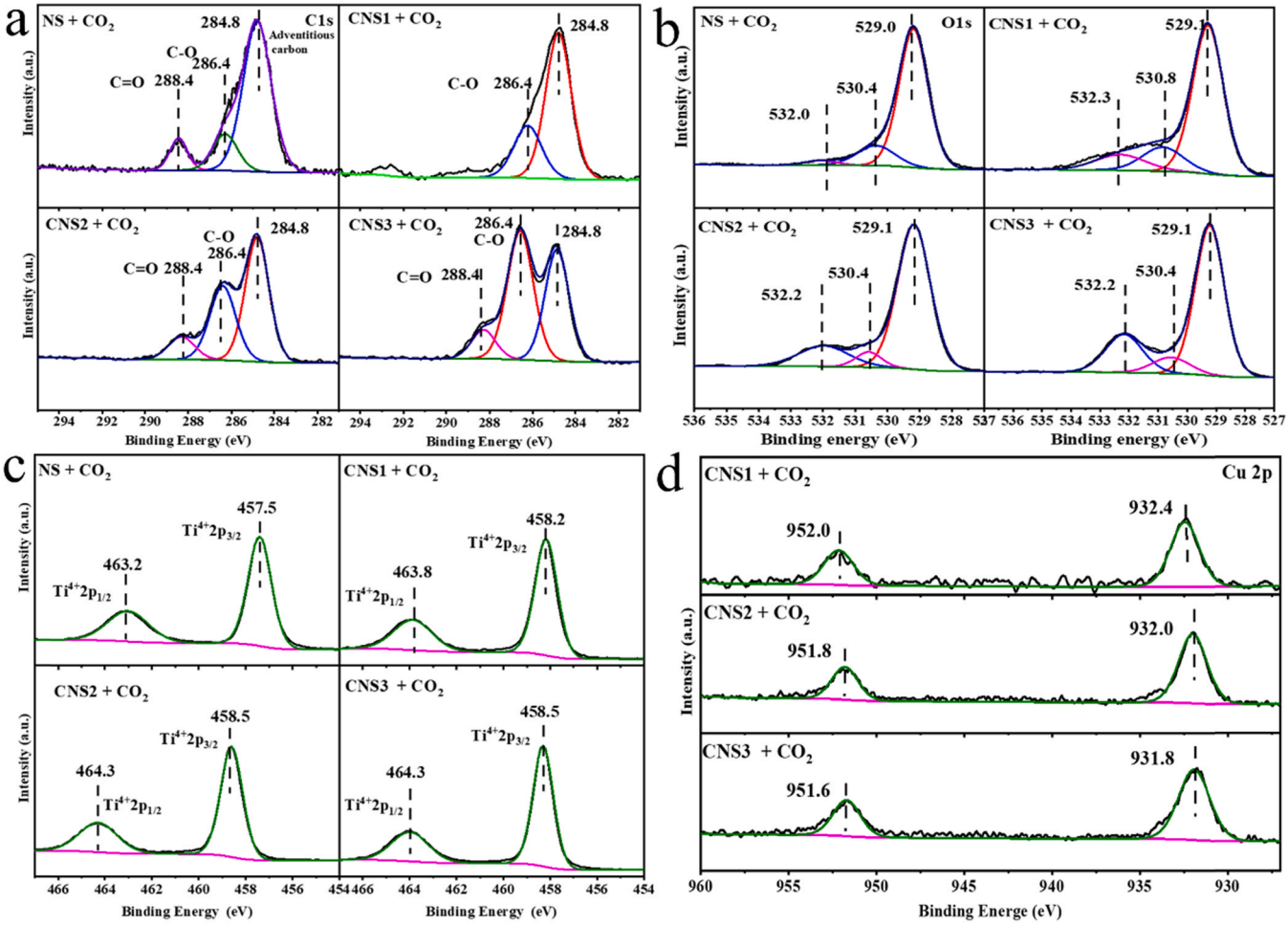

Fig. 5. XPS spectra of the samples after adsorption of CO_2. (a) C 1 s; (b) O 1 s; (c) Ti 2p; (d) Cu 2p.

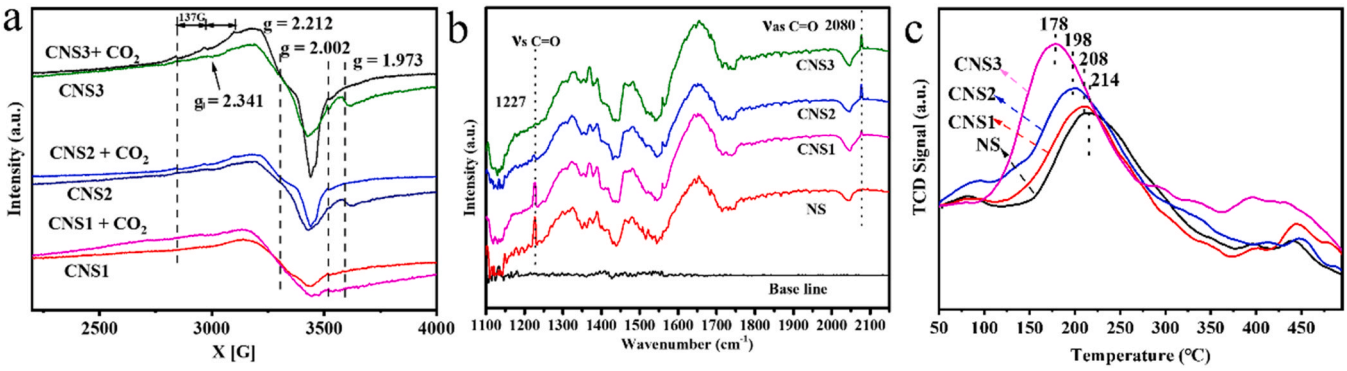

Fig. 6. (a) In situ EPR spectra of the samples in CO_2 atmosphere under the dark; (b) In situ FTIR spectra of the absorption for CO_2 over the samples; (c) CO_2-TPD for the catalysts.

In situ FT-IR was adopted out to further explore the coordination mode for CO_2. As shown in Fig. 6b, the peaks at 1227 cm^{-1} could be assigned to the asymmetrical stretching vibration of C═O bond in bridging Ti···CO_2^-···Ti species [15]. With increasing the mass of loaded Cu_2O, a new peak at 2080 cm^{-1} gradually appears in the spectra of CNSX but the peak at 1227 cm^{-1} disappears. It is reported that the peak (2080 cm^{-1}) may be considered as the symmetrical stretching vibration (C═O) of the CO* group [56]. Compared the vibration peak of C═O bond at 2365 cm^{-1} in free CO_2, this peak (2080 cm^{-1}) shifts to lower wavenumbers, implying that one C═O of CO_2 may be not involved in coordination. So, the bimetal bridging Cu···CO_2···Ti intermediate may be generated successfully on CNSX. In addition, the temperature-programmed desorption of CO_2 (CO_2-TPD) was used to further distinguish the bridging Ti···CO_2^-···Ti and bimetal bridging Cu···CO_2···Ti intermediate. Each sample only exhibits a main desorption peak at 214 (NS), 208 (CNS1), 198 (CNS2) and 178 ℃ (CNS3) in Fig. 6c, assigning to the adsorption CO_2 species. The hapticity of bridging Ti···CO_2^-···Ti intermediate (μ_2-η^4) is higher than that of the bimetal bridging Cu···CO_2···Ti (μ_1-η^2), suggesting that Ti···CO_2^-···Ti is more stable than Cu···CO_2···Ti [57]. Therefore, the decreased desorption

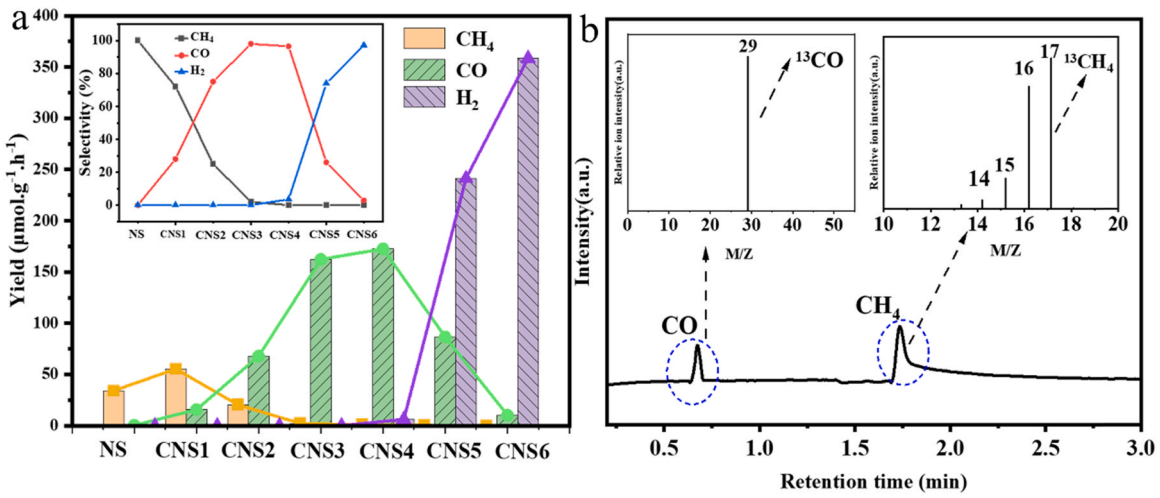

Fig. 7. (a) Photocatalytic performances of the catalysts. Reaction conditions: 10 mg catalyst, 20 mL H_2O, 1 atm CO_2 (99.999%), under Xe-lamp ($\lambda \geq 360$ nm); (b) GC-MS spectrum of the products after $^{13}CO_2$ photoreduction for CNS2, inset: signals of $m/z = 29$ (^{13}CO) and $m/z = 17$ ($^{13}CH_4$).

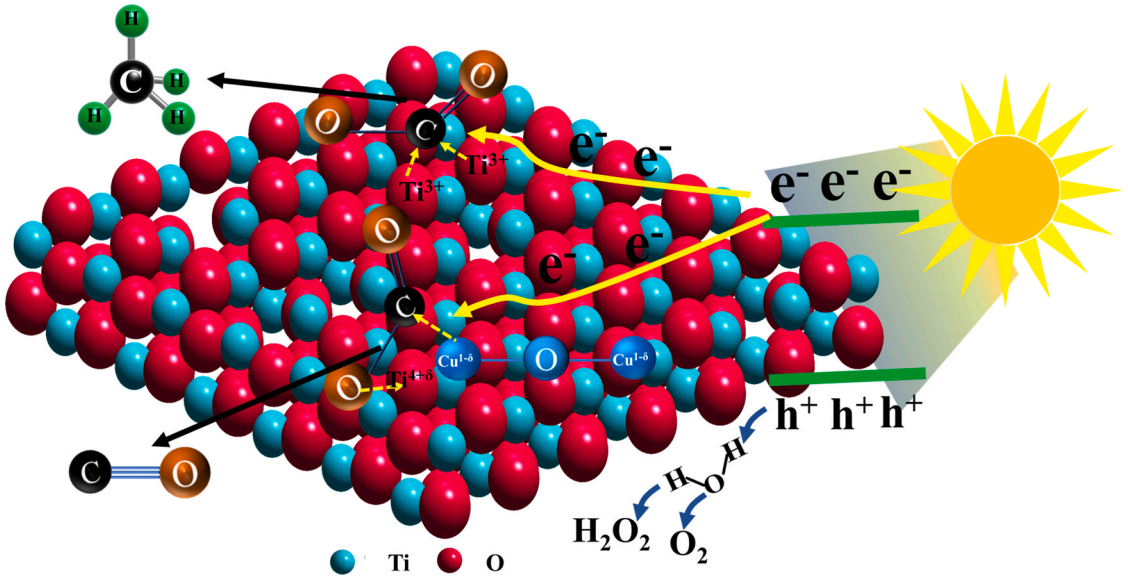

Fig. 8. Schematic illustration of proposed feasible mechanism for the photocatalytic reduction of CO_2.

temperature reveals that the coordination species have changed.

Based on above results, it could be concluded that the coordination mode on CNSX possesses C═O and C-O bonds. Moreover, the electrons transfer takes place between in CO_2 and active sites (O→$Ti^{4+\delta}$ and $Cu^{1-\delta}$→C). Hence, the bimetal bridging Cu···CO_2···Ti mode is generated assuredly on CNSX. Moreover, the bridging Ti···CO_2^-···Ti mode would disappear on the catalysts but the bimetal bridging Cu···CO_2···Ti appear gradually with increasing the mass of Cu_2O. Therefore, the products selectivity of CO and CH_4 could be governed effectively.

3.4. Mechanism of CO_2 photocatalytic reduction

Based on above results and discussion, a possible mechanism is discussed to elucidate CO and CH_4 generation pathway on the catalysts and further understand how the coordination mode determines the products selectivity. As shown in Fig. 8, under dark, CO_2 molecule would be bonded on the surface of catalyst. On NS surface, CO_2 can be absorbed via the formation of Ti···CO_2^-···Ti intermediate which facilitates CH_4 generation. However, on CNSX surface, Cu^+–Ti^{3+} interface interaction results in the formation of electron-deficient $Ti^{4+\delta}$ sites (LA) and electron-rich $Cu^{1-\delta}$ (LB) sites. So, the bimetal bridging Cu···CO_2···Ti species is formed via the charge transfer from O (CO_2) to $Ti^{4+\delta}$ and $Cu^{1-\delta}$ to C. Because of this bidirectional charge transfer, the activated CO_2 molecule may keep electric neutrality, which impedes the protonation of CO_2 and further makes the product toward to the production of CO. In addition, in this intermediate, only one C═O coordinates with the active sites, implying that the activated C═O is easier to be dissociated for generating CO. Under light, the catalysts and the charge transfer band would be excited to fleetly produce the photogenerated electrons. Then the electrons are quickly transferred to the coordinated CO_2 via the coordination bond. Finally, the generated CO and CH_4 split away off the catalyst. Meanwhile, the photogenerated holes may be consumed to produce H_2O_2 and O_2, which is discussed in our previous work [14].

4. Conclusion

In summary, the products selectivity of CH_4 and CO from photoreduction CO_2 is successfully controlled via creating Cu_2O clusters/TiO_2 ultrathin nanosheet as a photocatalyst, which is profited from the Cu^+-Ti^{3+} interface interaction to tailor the coordination mode of CO_2. The

Cu^{+}-Ti^{3+} interface interaction causes the generation of $Cu^{1-\delta}$ and $Ti^{4+\delta}$ sites and elimination of Ti^{3+} via the charge transfer from Ti^{3+} to Cu^{+}. In this case, the bimetal bridging Cu···CO_2···Ti species with coordination bonds (O→Ti and Cu→C) would be formed on CNSX, which determines the formation CO. Moreover, loading Cu_2O can improve the adsorption of visible light and the separation and transfer ability for generated carriers. The CO_2 coordination greatly increases the adsorption of visible light, which benefits from the excitation of the charge transfer band. The coordination bonds could accelerate the photogenerated electron transfer to CO_2 for generating the products. As a result, NS exhibits 100% selectivity of CH_4 (37.6 μmol g^{-1} h^{-1}) but CNS3 achieves 98% selectivity of CO (162.6 μmol g^{-1} h^{-1}). This work may provide a special horizon to tailor the products selectivity from photoreduction CO_2 via the interface interaction mediated the CO_2 coordination mode.

CRediT authorship contribution statement

Zhi-Wen Wang: Conceptualization, Investigation, Formal analysis. **Ying-Zhang Shi**: Validation, Formal analysis. **Yue-Yue Kang**: Formal analysis, **Cheng Liu**: Software. Data curation. **Ling Wu:** Conceptualization, Writing – review & editing.

Declaration of Competing Interest

The authors declare that they have no known competing financial interests or personal relationships that could have appeared to influence the work reported in this paper.

Acknowledgments

This work was supported by the National Natural Science Foundation of China (21872032).

Appendix A. Supporting information

Supplementary data associated with this article can be found in the online version at doi:10.1016/j.apcatb.2021.120803.

References

[1] C. Das Neves Gomes, O. Jacquet, C. Villiers, P. Thuéry, M. Ephritikhine, T. Cantat, A diagonal approach to chemical recycling of carbon dioxide: organocatalytic transformation for the reductive functionalization of CO_2, Angew. Chem. Int. Ed. 51 (2012) 187–190, https://doi.org/10.1002/anie.201105516.

[2] Y. Dong, P. Duchesne, A. Mohan, K.K. Ghuman, P. Kant, L. Hurtado, U. Ulmer, J.Y. Y. Loh, A.A. Tountas, L. Wang, A. Jelle, M. Xia, R. Dittmeyer, G.A. Ozin, Shining light on CO_2: from materials discovery to photocatalyst, photoreactor and process engineering, Chem. Soc. Rev. 49 (2020) 951–982, https://doi.org/10.1039/d0cs00597e.

[3] S. Kreft, R. Schoch, J. Schneidewind, J. Rabeah, E.V. Kondratenko, V. A. Kondratenko, H. Junge, M. Bauer, S. Wohlrab, M. Beller, Improving selectivity and activity of CO_2 reduction photocatalysts with oxygen, Chem 5 (2019) 1818–1833, https://doi.org/10.1016/j.chempr.2019.04.006.

[4] Z. Sun, H. Wang, Z. Wu, L. Wang, g-C_3N_4 based composite photocatalysts for photocatalytic CO_2 reduction, Catal. Today 300 (2018) 160–172, https://doi.org/10.1016/j.cattod.2017.05.033.

[5] A. Modak, P. Bhanja, S. Dutta, B. Chowdhury, A. Bhaumik, Catalytic reduction of CO_2 into fuels and fine chemicals, Green. Chem. 22 (2020) 4002–4033, https://doi.org/10.1039/d0gc01092h.

[6] J. Albero, Y. Peng, H. García, Photocatalytic CO_2 reduction to C_{2+} products, ACS Catal. 10 (2020) 5734–5749, https://doi.org/10.1021/acscatal.0c00478.

[7] S.N. Habisreutinger, L. Schmidt-Mende, J.K. Stolarczyk, Photocatalytic reduction of CO_2 on TiO_2 and other semiconductors, Angew. Chem. Int. Ed. 52 (2013) 7372–7408, https://doi.org/10.1002/anie.201207199.

[8] J. Wang, S. Lin, N. Tian, T. Ma, Y. Zhang, H. Huang, Nanostructured metal sulfides: classification, modification strategy, and solar-driven CO_2 reduction application, Adv. Funct. Mater. 31 (2021) 1–39, https://doi.org/10.1002/adfm.202008008.

[9] Y.Y. Birdja, E. Perez-Gallent, M.C. Figueiredo, A.J. Göttle, F. Calle-Vallejo, M.T. M. Koper, Advances and challenges in understanding the electrocatalytic conversion of carbon dioxide to fuels, Nat. Energy 4 (2019) 732–745, https://doi.org/10.1038/s41560-019-0450-y.

[10] S. Ali, A. Razzaq, H. Kim, S.-I. In, Activity, selectivity and stability of the earth abundant CuO/Cu_2O/Cu0 based photocatalysts towards photocatalytic CO_2 reduction, Chem. Eng. J. (2021), 131579, https://doi.org/10.1016/j.cej.2021.131579.

[11] J. Fu, K. Jiang, X. Qiu, J. Yu, M. Liu, Product selectivity of photocatalytic CO_2 reduction reactions, Mater. Today 32 (2020) 222–243, https://doi.org/10.1016/j.mattod.2019.06.009.

[12] S. Hennessey, P. Farràs, Production of solar chemicals: gaining selectivity with hybrid molecule/semiconductor assemblies, Chem. Commun. 54 (2018) 6662–6680, https://doi.org/10.1039/c8cc02487a.

[13] Y. Wang, J. Liu, Y. Wang, A.M. Al-Enizi, G. Zheng, Tuning of CO_2 reduction selectivity on metal electrocatalysts, Small 13 (2017) 1–15, https://doi.org/10.1002/smll.201701809.

[14] X. Chang, T. Wang, J. Gong, CO_2 photo-reduction: Insights into CO_2 activation and reaction on surfaces of photocatalysts, Energy Environ. Sci. 9 (2016) 2177–2196, https://doi.org/10.1039/c6ee00383d.

[15] Z. Wang, Q. Wan, Y. Shi, H. Wang, Y. Kang, S. Zhu, S. Lin, L. Wu, Selective photocatalytic reduction CO_2 to CH_4 on ultrathin TiO_2 nanosheet via coordination activation, Appl. Catal. B Environ. 288 (2021), 120000, https://doi.org/10.1016/j.apcatb.2021.120000.

[16] X. Li, J. Yu, M. Jaroniec, X. Chen, Cocatalysts for selective photoreduction of CO_2 into solar fuels, Chem. Rev. 119 (2019) 3962–4179, https://doi.org/10.1021/acs.chemrev.8b00400.

[17] S.L. Wang, X. Luo, X. Zhou, Y. Zhu, X. Chi, W. Chen, K. Wu, Z. Liu, S.Y. Quek, G. Q. Xu, Fabrication and properties of a free-standing two-dimensional titania, J. Am. Chem. Soc. 139 (2017) 15414–15419, https://doi.org/10.1021/jacs.7b08229.

[18] Z. He, L. Wen, D. Wang, Y. Xue, Q. Lu, C. Wu, J. Chen, S. Song, Photocatalytic reduction of CO_2 in aqueous solution on surface-fluorinated anatase TiO_2 nanosheets with exposed {001} facets, Energy Fuels 28 (2014) 3982–3993, https://doi.org/10.1021/ef500648k.

[19] N. Roy, Y. Sohn, D. Pradhan, Synergy of low-energy {101} and high-energy {001} TiO_2 crystal facets for enhanced photocatalysis, ACS Nano 7 (2013) 2532–2540, https://doi.org/10.1021/nn305877v.

[20] Y. Bessekhouad, D. Robert, J.V. Weber, Photocatalytic activity of Cu_2O/TiO_2, Bi_2O_3/TiO_2 and $ZnMn_2O_4/TiO_2$ heterojunctions, Catal. Today 101 (2005) 315–321, https://doi.org/10.1016/j.cattod.2005.03.038.

[21] S.M. Park, A. Razzaq, Y.H. Park, S. Sorcar, Y. Park, C.A. Grimes, S.-I. In, Hybrid Cu_xO-TiO_2 heterostructured composites for photocatalytic CO_2 reduction into methane using solar irradiation: sunlight into fuel, ACS Omega 1 (2016) 868–875, https://doi.org/10.1021/acsomega.6b00164.

[22] S.C. Wu, C.S. Tan, M.H. Huang, Strong facet effects on interfacial charge transfer revealed through the examination of photocatalytic activities of various Cu_2O–ZnO heterostructures, Adv. Funct. Mater. 27 (2017), https://doi.org/10.1002/adfm.201604635.

[23] X. An, K. Li, J. Tang, Cu_2O/reduced graphene oxide composites for the photocatalytic conversion of CO_2, ChemSusChem 7 (2014) 1086–1093, https://doi.org/10.1002/cssc.201301194.

[24] C. Huang, W. Ye, Q. Liu, X. Qiu, Dispersed Cu_2O octahedrons on h-BN nanosheets for p -Nitrophenol reduction, ACS Appl. Mater. Interfaces 6 (2014) 14469–14476, https://doi.org/10.1021/am5037737.

[25] P. Karthik, E. Balaraman, B. Neppolian, Efficient solar light-driven H_2 production: post-synthetic encapsulation of a Cu_2O co-catalyst in a metal-organic framework (MOF) for boosting the effective charge carrier separation, Catal. Sci. Technol. 8 (2018) 3286–3294, https://doi.org/10.1039/c8cy00604k.

[26] Y. Wang, S. Deng, B. Liu, Y. Jin, Mechanistic understanding on the role of Cu species over the CuOx/TiO_2 catalyst for CO_2 photoreduction, ACS Omega 5 (2020) 18050–18063, https://doi.org/10.1021/acsomega.0c01533.

[27] M.E. Aguirre, R. Zhou, A.J. Eugene, M.I. Guzman, M.A. Grela, Cu_2O/TiO_2 heterostructures for CO_2 reduction through a direct Z-scheme: Protecting Cu_2O from photocorrosion, Appl. Catal. B Environ. 217 (2017) 485–493, https://doi.org/10.1016/j.apcatb.2017.05.058.

[28] X. Zhao, Y. Fan, W. Zhang, X. Zhang, D. Han, L. Niu, A. Ivaska, Nanoengineering construction of Cu_2O nanowire arrays encapsulated with g-C_3N_4 as 3D spatial reticulation all-solid-state direct Z-scheme photocatalysts for photocatalytic reduction of carbon dioxide, ACS Catal. 10 (2020) 6367–6376, https://doi.org/10.1021/acscatal.0c01033.

[29] L.D.M. Torquato, F.A.C. Pastrian, J.A.L. Perini, K. Irikura, A.P. Ana, A.G.S. de Oliveira-Filho, S.I. Córdoba de Torresi, M.V.B. Zanoni, Relation between the nature of the surface facets and the reactivity of Cu_2O nanostructures anchored on TiO_2NT@PDA electrodes in the photoelectrocatalytic conversion of CO_2 to methanol, Appl. Catal. B Environ. 261 (2020), 118221, https://doi.org/10.1016/j.apcatb.2019.118221.

[30] S. Qamar, F. Lei, L. Liang, S. Gao, K. Liu, Y. Sun, W. Ni, Y. Xie, Ultrathin TiO_2 flakes optimizing solar light driven CO_2 reduction, Nano Energy 26 (2016) 692–698, https://doi.org/10.1016/j.nanoen.2016.06.029.

[31] H. Shang, X. Wang, H. Li, M. Li, C. Mao, P. Xing, S. Zhao, Z. Chen, J. Sun, Z. Ai, L. Zhang, Oxygen vacancies promote sulfur species accumulation on TiO_2 mineral particles, Appl. Catal. B Environ. 290 (2021), 120024, https://doi.org/10.1016/j.apcatb.2021.120024.

[32] Y. Li, W.N. Wang, Z. Zhan, M.H. Woo, C.Y. Wu, P. Biswas, Photocatalytic reduction of CO_2 with H_2O on mesoporous silica supported Cu/TiO_2 catalysts, Appl. Catal. B Environ. 100 (2010) 386–392, https://doi.org/10.1016/j.apcatb.2010.08.015.

[33] L. Hurtado, R. Natividad, H. García, Photocatalytic activity of Cu_2O supported on multi layers graphene for CO_2 reduction by water under batch and continuous flow, Catal. Commun. 84 (2016) 30–35, https://doi.org/10.1016/j.catcom.2016.05.025.

[34] T. Wei, Y.N. Zhu, X. An, L.M. Liu, X. Cao, H. Liu, J. Qu, Defect modulation of Z-scheme TiO_2/Cu_2O photocatalysts for durable water splitting, ACS Catal. 9 (2019) 8346–8354, https://doi.org/10.1021/acscatal.9b01786.
[35] M. Wang, L. Sun, Z. Lin, J. Cai, K. Xie, C. Lin, P-n Heterojunction photoelectrodes composed of Cu_2O-loaded TiO_2 nanotube arrays with enhanced photoelectrochemical and photoelectrocatalytic activities, Energy Environ. Sci. 6 (2013) 1211–1220, https://doi.org/10.1039/c3ee24162a.
[36] W. Wang, X. Huang, S. Wu, Y. Zhou, L. Wang, H. Shi, Y. Liang, B. Zou, Preparation of p-n junction $Cu_2O/BiVO_4$ heterogeneous nanostructures with enhanced visible-light photocatalytic activity, Appl. Catal. B Environ. 134–135 (2013) 293–301, https://doi.org/10.1016/j.apcatb.2013.01.013.
[37] D. Tan, J. Zhang, J. Shi, S. Li, B. Zhang, X. Tan, F. Zhang, L. Liu, D. Shao, B. Han, Photocatalytic CO_2 transformation to CH_4 by Ag/Pd bimetals supported on NDoped TiO_2 nanosheet, ACS Appl. Mater. Interfaces 10 (2018) 24516–24522, https://doi.org/10.1021/acsami.8b06320.
[38] Y. Ren, J. Zou, K. Jing, Y. Liu, B. Guo, Y. Song, Y. Yu, L. Wu, Photocatalytic synthesis of N-benzyleneamine from benzylamine on ultrathin BiOCl nanosheets under visible light, J. Catal. 380 (2019) 123–131, https://doi.org/10.1016/j.jcat.2019.10.018.
[39] Y. Song, H. Wang, J. Xiong, B. Guo, S. Liang, L. Wu, Photocatalytic hydrogen evolution over monolayer $H_{1.07}Ti_{1.73}O_4$ H_2O nanosheets: roles of metal defects and greatly enhanced performances, Appl. Catal. B Environ. 221 (2018) 473–481, https://doi.org/10.1016/j.apcatb.2017.09.009.
[40] F. Gonell, A.V. Puga, B. Julián-López, H. García, A. Corma, Copper-doped titania photocatalysts for simultaneous reduction of CO_2 and production of H_2 from aqueous sulfide, Appl. Catal. B Environ. 180 (2016) 263–270, https://doi.org/10.1016/j.apcatb.2015.06.019.
[41] S. Ali, J. Lee, H. Kim, Y. Hwang, A. Razzaq, J.W. Jung, C.H. Cho, S. Il In, Sustained, photocatalytic CO_2 reduction to CH_4 in a continuous flow reactor by earth-abundant materials: reduced titania-Cu_2O Z-scheme heterostructures, Appl. Catal. B Environ. 279 (2020), 119344, https://doi.org/10.1016/j.apcatb.2020.119344.
[42] W. Guo, J. Zou, B. Guo, J. Xiong, C. Liu, Z. Xie, L. Wu, Pd nanoclusters/TiO_2(B) nanosheets with surface defects toward rapid photocatalytic dehalogenation of polyhalogenated biphenyls under visible light, Appl. Catal. B Environ. 277 (2020), 119255, https://doi.org/10.1016/j.apcatb.2020.119255.
[43] T. Gao, H. Fjellvaåg, P. Norby, Defect chemistry of a zinc-doped lepidocrocite titanate $CS_xTi_{2-x}/2Zn_{x/2}O_4$ (x = 0.7) and its protonic form, Chem. Mater. 21 (2009) 3503–3513, https://doi.org/10.1021/cm901329g.
[44] S. Zhu, X. Chen, Z. Li, X. Ye, Y. Liu, Y. Chen, L. Yang, M. Chen, D. Zhang, G. Li, H. Li, Cooperation between inside and outside of TiO_2: Lattice Cu^+ accelerates carrier migration to the surface of metal copper for photocatalytic CO_2 reduction, Appl. Catal. B Environ. 264 (2020), 118515, https://doi.org/10.1016/j.apcatb.2019.118515.
[45] C. Dennison, Investigating the structure and function of cupredoxins, in: Coord. Chem. Rev, 249, 2005, pp. 3025–3054, https://doi.org/10.1016/j.ccr.2005.04.021.
[46] L. Liu, Y. Jiang, H. Zhao, J. Chen, J. Cheng, K. Yang, Y. Li, Engineering coexposed {001} and {101} facets in oxygen-deficient TiO_2 nanocrystals for enhanced CO_2 photoreduction under visible light, ACS Catal. 6 (2016) 1097–1108, https://doi.org/10.1021/acscatal.5b02098.
[47] Y. Chen, S. Ji, W. Sun, Y. Lei, Q. Wang, A. Li, W. Chen, G. Zhou, Z. Zhang, Y. Wang, L. Zheng, Q. Zhang, L. Gu, X. Han, D. Wang, Y. Li, Engineering the atomic interface with single platinum atoms for enhanced photocatalytic hydrogen production, Angew. Chem. Int. Ed. 59 (2020) 1295–1301, https://doi.org/10.1002/anie.201912439.
[48] Y. Liu, C. Miao, P. Yang, Y. He, J. Feng, D. Li, Synergetic promotional effect of oxygen vacancy-rich ultrathin TiO_2 and photochemical induced highly dispersed Pt for photoreduction of CO_2 with H_2O, Appl. Catal. B Environ. 244 (2019) 919–930, https://doi.org/10.1016/j.apcatb.2018.12.028.
[49] H. Zhu, Z. Qin, W. Shan, W. Shen, J. Wang, Pd/CeO_2-TiO_2 catalyst for CO oxidation at low temperature: a TPR study with H_2 and CO as reducing agents, J. Catal. 225 (2004) 267–277, https://doi.org/10.1016/j.jcat.2004.04.006.
[50] N. Riaz, M.A. Bustam, F.K. Chong, Z.B. Man, M.S. Khan, A.M. Shariff, Photocatalytic degradation of DIPA using bimetallic Cu-Ni/TiO_2 photocatalyst under visible light irradiation, Sci. World J. 2014 (2014), 342020, https://doi.org/10.1155/2014/342020.
[51] H. Romar, A.H. Lillebo, P. Tynjala, T. Hu, A. Holmen, E.A. Blekkan, U. Lassi, H_2-TPR, XPS and TEM Study of the Reduction of Ru and Re promoted Co/γ-Al_2O_3, Co/TiO_2 and Co/SiC catalysts, J. Mater. Sci. Res 5 (2016) 39, https://doi.org/10.5539/jmsr.v5n2p39.
[52] C. Baldacchini, A.R. Bizzarri, S. Cannistraro, Excitation of the ligand-to-metal charge transfer band induces electron tunnelling in azurin, Appl. Phys. Lett. 104 (2014) 53–56, https://doi.org/10.1063/1.4867884.
[53] H. Kunkely, A. Vogler, Generation of nitric oxide by photolysis of silver hyponitrite in suspension induced by LMCT excitation, Inorg. Chem. Commun. 10 (2007) 1294–1296, https://doi.org/10.1016/j.inoche.2007.07.017.
[54] Y.A. Wu, I. McNulty, C. Liu, K.C. Lau, Q. Liu, A.P. Paulikas, C.J. Sun, Z. Cai, J. R. Guest, Y. Ren, V. Stamenkovic, L.A. Curtiss, Y. Liu, T. Rajh, Facet-dependent active sites of a single Cu_2O particle photocatalyst for CO_2 reduction to methanol, Nat. Energy 4 (2019) 957–968, https://doi.org/10.1038/s41560-019-0490-3.
[55] M.C.R. Symons, D.X. West, J.G. Wilkinson, Co-ordination of copper(II) ions doped in pentacyanonitrosylferrate(2-) and tetrathiocyanatometallate(II) salts: an electron spin resonance study, J. Chem. Soc. Dalton Trans. 16 (1975) 1696–1700.
[56] X. Li, Y. Sun, J. Xu, Y. Shao, J. Wu, X. Xu, Y. Pan, H. Ju, J. Zhu, Y. Xie, Selective visible-light-driven photocatalytic CO_2 reduction to CH_4 mediated by atomically thin $CuIn_5S_8$ layers, Nat. Energy 4 (2019) 690–699, https://doi.org/10.1038/s41560-019-0431-1.
[57] A. Falceto, E. Carmona, S. Alvarez, Electronic and structural effects of low-hapticity coordination of arene rings to transition metals, Organometallics 33 (2014) 6660–6668, https://doi.org/10.1021/om5009583.